

Scalability enhancement of quantum computing under limited connectivity through distributed quantum computing

Shao-Hua Hu,¹ George Biswas,^{1,2} and Jun-Yi Wu^{1,2,3,*}

¹*Department of Physics, Tamkang University, New Taipei 25137, Taiwan, ROC*

²*Center for Advanced Quantum Computing, Tamkang University, New Taipei 25137, Taiwan, ROC*

³*Physics Division, National Center for Theoretical Sciences, Taipei 10617, Taiwan, ROC*

Abstract

We employ quantum-volume random-circuit sampling to benchmark the two-QPU entanglement-assisted distributed quantum computing (DQC), and compare it with single-QPU quantum computing. We first specify a single-qubit depolarizing noise model in the random circuit. Based on this error model, we show the one-to-one correspondence of three figures of merits, namely average gate fidelity, heavy output probability, and linear cross-entropy. We derive an analytical approximation of the average gate fidelity under the specified noise model, which is shown to align with numerical simulations. The approximation is calculated based on an allocation matrix obtained from the extended connectivity graph of a DQC device. In numerical simulation, we unveil the scalability enhancement in DQC for the QPUs with limited connectivity. Furthermore, we provide a simple formula to estimate the average gate fidelity, which also provides us with a heuristic method to evaluate the scalability enhancement in DQC, and a guide to optimize the structure of a DQC configuration.

I. INTRODUCTION

In noisy intermediate-scale quantum (NISQ) computing, the imperfection on quantum processing units (QPUs) can not yet be corrected. The defects on a single QPU are much more difficult to suppress as the number of qubits increases, which limits the scalability of quantum computers. A solution for scaling up quantum computers is distributed quantum computing (DQC) [1, 2], in which one implements global quantum circuits over multiple high-quality small-size QPUs.

The ultimate goal of DQC is to scale up quantum computing by connecting multiple QPUs. Explicitly, one aims to implement a global unitary assisted by classical and quantum communication across different QPUs, rather than direct nonlocal gates. In general, DQC can be classified into two types according to the principle of connections between two QPUs. The first type of DQC employs only local operations and classical communication (LOCC), which is called circuit knitting [3–7]. The second type of DQC is called entanglement-assisted DQC, which employs quantum communication to share entanglement between QPUs and implement entanglement-assisted LOCC, such as state teleportation [8] or telegating [9–16]. In this paper, we consider the entanglement-assisted DQC, since the circuit knitting, has the problem of the computational overhead.

To verify the enhancement of computation power in DQC, one needs to benchmark and compare the quantum computing power of multi-QPU DQC devices and single-QPU devices. The corresponding figures of merits include average gate fidelity (AGF)[17], heavy output probability (HOP)[18], and linear cross-entropy (LXE)[19]. The quality of the quantum computing on a quantum processor can be then quantified by averaging these fig-

ures of merits over a random sampling of quantum circuits. In [18], a randomized benchmarking based on HOP is introduced to quantify the maximum scale of a sub-collection of qubits of a QPU that allows quantum advantage, which is called the quantum volume (QV) of a QPU. The original approach of QV benchmarking is a heavy output generation test [20] based on QV random circuits.

In this paper, we adopt different figures of merits (AGF, HOP, and LXE) to the QV random-circuit sampling, and extend it to two-QPU DQC. The extended benchmarking allows us to reveal the scalability enhancement of quantum computing in DQC. To verify scalability enhancement in DQC, we simulate and compare the QV benchmarking for both single-QPU quantum computing and two-QPU DQC. By definition, the average gate fidelity quantifies the faithfulness of the quantum operations implemented by a quantum device, while the heavy output probability and linear cross entropy only indicate the closeness of the measurement outputs and the ideal ones. However, since the measurement complexity of average gate fidelity increases exponentially with the system size [21], it is even experimentally impossible to evaluate average gate fidelity on a quantum computer. In contrast, the evaluation of heavy output probability and linear cross-entropy can be experimentally implemented with random circuit samplings.

In this paper, we show the one-to-one correspondence among average AGF \bar{F} , HOP \bar{H} , and LXE $\bar{\chi}$ in the QV random-circuit benchmarking under an approximated error model

$$\bar{F} \xleftrightarrow{\text{QV random}} \bar{H} \xleftrightarrow{\text{QV random}} \bar{\chi}. \quad (1)$$

This result allows us to estimate average gate fidelity from heavy output probability or linear cross-entropy in numerical simulation, and vice versa calculate heavy output probability and linear cross-entropy via average gate fidelity. Employing average AGF \bar{F} as the figure of merit, we derive an approximated formula of \bar{F}

* junyiwu.physics@gmail.com

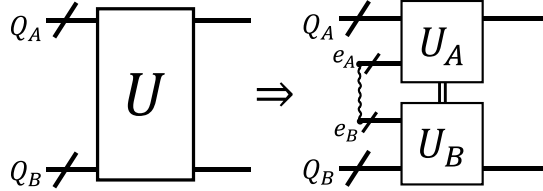


FIG. 1. Implementation of a global unitary U over two QPUs Q_A and Q_B through local unitaries U_A and U_B , with the help of pre-shared entangled pairs e_{AB} (wiggly line) and classical communications (double line).

for the QV random-circuit benchmarking of multi-QPU DQC devices under arbitrary connectivity described by extended connectivity graphs. The theory of error model approximation is supported by numerical simulations on qiskit. Our numerical simulations also show evidence of better average AGF of two-QPU DQC devices surpassing single-QPU devices

$$\bar{F}_{DQC} \geq \bar{F}_{single}. \quad (2)$$

It therefore shows the scalability enhancement of DQC under limited qubit connectivity in QPUs.

The paper is constructed as follows. In Section II, we review the concept of entanglement-assisted DQC, random-circuit benchmarking, and qubit connectivity. In Section III, we model the noises in random-circuit sampling by an approximation with single-qubit depolarizing channels, show the one-to-one correspondence among AGF, HOP, and LXE, and derive an analytical formula for average AGF. In Section IV, we implement numerical simulations of the QV random-circuit benchmarking and unveil the evidence for the scalability enhancement of two-QPU DQC with limited connectivity. In the end, we discuss our results in Section V and conclude the paper in Section VI.

II. PRELIMINARY

A. Entanglement-assisted DQC

In two-QPU entanglement-assisted DQC, one aims to execute a large quantum circuit over two small-size QPUs through local operations assisted by classical communication and pre-shared entangled pairs, i.e. entanglement-assisted LOCC, as shown in Figure 1.

A promising tool for achieving this is Quantum state teleportation. Quantum state teleportation is a special quantum operation that transfers a quantum state from one location to another using an entangled pair (also

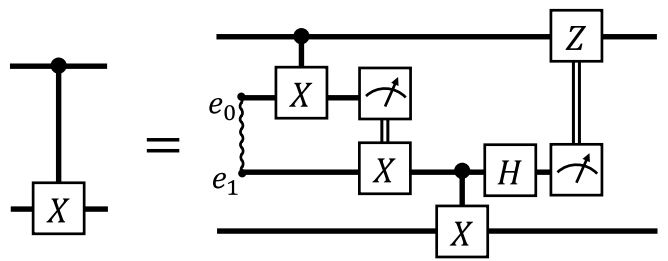


FIG. 2. Implementation of a non-local CNOT gate using the EJPP protocol. The two central qubits are auxiliary qubits that share a maximally entangled pair represented by a wiggly line. Here we use the Bell state $|\Phi^+\rangle \equiv \frac{1}{\sqrt{2}}(|00\rangle + |11\rangle)$.

known as a Bell state) and local operations with classical communication (LOCC) [22]. Instead of directly sending the quantum state, it exploits entanglement and classical communication to transfer the state. Expanding on this concept, there's a similar idea called gate teleportation or telegate [9, 13]. This proposes that the CNOT gate, a crucial quantum gate, can be executed locally using an entangled pair and LOCC. Specifically, a protocol known as the EJPP protocol (named after its creators) was introduced for this purpose [9].

The EJPP protocol's circuit, depicted in Figure 2, illustrates how this telegating protocol works in practice. It enables the execution of CNOT gates across different QPUs through the clever use of entanglement and classical communication, allowing for the distributed execution of quantum circuits.

It is known that the CNOT gate is the only two-qubit gate in the universal set. Therefore, with the EJPP protocol, universal quantum computing can be implemented across multiple QPUs.

In our study, we aim to enhance quantum computer capabilities through DQC. We assume local QPUs have unlimited access to entangled pairs, although creating them remains challenging. Therefore, while our focus is on maximizing computational power, we also recognize the importance of minimizing entangled pair usage in circuit implementation, a topic deserving its discussion [15].

B. Benchmarking via random-circuit sampling

To validate quantum computational power, one needs a systematic benchmarking method to verify the computation on a quantum computing device. One such benchmarking method relies on random circuit sampling, demonstrating quantum advantage by comparing outcome distributions between theoretical predictions and experimental results [20]. Ideally, one would sample circuits randomly over the Haar measure [23], representing a unitary invariant uniform distribution of unitary transformation. In a practical randomized benchmarking protocol, we need random circuits that are approximately

random unitaries under Haar measure. Prominent examples include quantum volume (QV) benchmarking[18] and cross-entropy (LXE) benchmarking[19].

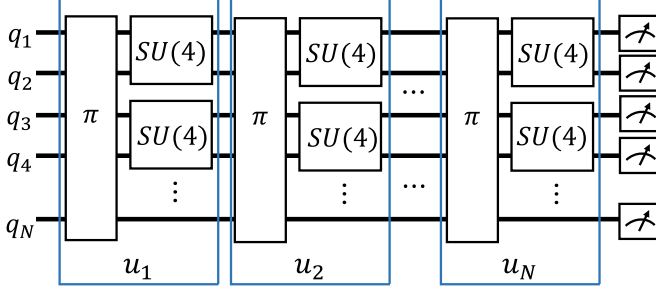


FIG. 3. An N -qubit random circuit in quantum volume benchmarking. Each layer u_i consists of a random permutation gate π and several 2-qubit Haar random $SU(4)$ gates.

In the QV benchmarking, which is illustrated in Fig. 3, an N -qubit benchmarking circuit is constituted by N layers of gates. Each layer comprises a random permutation gate π and random 2-qubit $SU(4)$ gates sampled under the Haar measure. To avoid unnecessary noises introduced by permutation gates, one can randomly reposition the $SU(4)$ gates instead of random permutation gates.

For a U generated from a randomly sampled circuit,

$$U = u_N \cdot u_{N-1} \cdots u_2 \cdot u_1, \quad (3)$$

one calculates the theoretical distribution of outputs $q_U(x) \equiv |\langle x|U|0 \rangle|^2$ on classical computers, and labels an output x as heavy, if its probability $p_U(x)$ is greater than the median of the distribution. We denote the set of heavy outputs as X_U , which contains 2^{N-1} elements. The HOP H_U is then defined as the summation of the probabilities of all heavy outputs:

$$H_U \equiv \sum_{x \in X_U} q_U(x), \quad X_U \equiv \{x \text{ is heavy output of } U\}. \quad (4)$$

The average HOP converges to $\frac{1+\ln 2}{2}$ (≈ 0.85), for the ideal devices and it is 0.5 for the completely depolarized devices.

In the linear cross-entropy benchmarking, we calculate the linear cross-entropy χ_U between the ideal probability distribution $q_U(x)$ and the tested probability distribution $p_U(x)$ measured from the testing device, which is defined as follows,

$$\chi_U \equiv 2^N \sum_{x \in \{0,1\}^N} p_U(x) q_U(x) - 1. \quad (5)$$

Besides HOP and LXE, the average gate fidelity (AGF) $F(U, \Lambda)$ [17] between the target unitary U and its implementation Λ_U on a real device is another figure of merit

for quantifying the performance of QPUs, which is defined as follows

$$F(U, \Lambda_U) = \int_{\Psi} d\psi \langle \psi | U^\dagger \Lambda_U(|\psi\rangle \langle \psi|) U | \psi \rangle, \quad (6)$$

where Ψ is the set of pure states under the Haar measure. The vectorization representation of a quantum state [24] is convenient for the calculation of AGF. In the vectorization representation, one defines a vectorized state of a density matrix ρ as follows,

$$|\rho\rangle\rangle \equiv (\rho \otimes \mathbb{I}) \sum_i |i\rangle \otimes |i\rangle. \quad (7)$$

For a pure state $\rho = |\psi\rangle\langle\psi|$, its vectorization is $|\psi\rangle\rangle \equiv |\psi\rangle \otimes |\psi\rangle^*$. In such vectorization presentation, a unitary operator becomes

$$\hat{U} \equiv U \otimes U^*. \quad (8)$$

With such vectorization the AGF of U is

$$F(U, \Lambda_U) \equiv \int_{\Psi} d\psi \langle \langle \psi | \hat{U}^\dagger \tilde{\Lambda}_U | \psi \rangle \rangle, \quad (9)$$

where $\tilde{\Lambda}_U$ is the noise quantum channel of the implementation of the target unitary U . Note that, in this paper, we employ the “hat” and “tilde” symbols to indicate the vectorization representation of a unitary and a quantum channel, respectively. In randomized benchmarking, the circuits are sampled from a set of random circuits \mathbb{U}_{RC} , one therefore should further average the AGF $F(U, \Lambda_U)$ over all the possible circuits as follows,

$$\bar{F} \equiv \int_{\mathbb{U}_{RC}} dU F(U, \Lambda_U). \quad (10)$$

We will employ these three figures of merit to evaluate the performance of DQC in the QV random-circuit-sampling test.

C. Connectivity of QPUs

The connectivity constraint is a common limitation for a QPU, which prevents direct implementation of a two-qubit gate on arbitrary pairs of qubit due to lack of direct physical coupling. The connectivity of a QPU can be represented by a graph with its edge indicating allowed two-qubit couplings. For a DQC device, which is composed of multiple QPUs, one can establish quantum channels sharing entanglement among qubits across the QPUs. The topology of quantum channels in DQC device can be also represented as a graph, in which a wiggly edge indicates a pair of shared entanglement. We extend the connectivity graph for single-QPU device to multi-QPU DQC device by combining local connectivity (solid lines) and the cross-QPU quantum channels (wiggly lines) in Fig. 4.

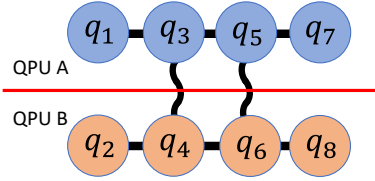


FIG. 4. The extended connectivity graph of a two-QPU DQC device, which has two local QPUs with 4 qubits on each. The solid lines denote direct physical couplings in local QPUs, while the wiggly lines stand for quantum channels across QPUs.

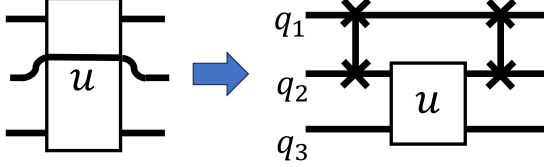


FIG. 5. The implementation of a two-qubit gate on two non-connected qubits q_1 and q_3 with two additional swap-gates.

On a single QPU, to overcome local connectivity limitations, a common approach is to apply additional swap gates, as illustrated in Figure 5. For high-quality performance of quantum computation under connectivity limitation, one needs to reduce the additional noises through the minimization of the swapping gates in the compilation of quantum circuits. Such a minimization process is called qubit allocation or assignment [25]. However, even with the optimal qubit allocation, for some types of physical qubits such as superconducting qubits, the average steps of swapping among qubits in the connectivity graph of a single QPU increases very quickly as the number of qubits gets larger.

One benefit of multi-QPU DQC is that it changes and enhances the connectivity of quantum computing devices, as we can use entangled pairs shared in the quantum channels between two QPUs to reshape the connectivity graph. The effect of such connectivity changes in DQC will be discussed in details in the remaining sections.

III. THE ERROR MODEL FOR RANDOM-CIRCUIT BENCHMARKING

Establishing a noise model is essential for the characterization of errors in quantum devices. In the QV random-circuit sampling, the two-qubit gates are sampled from Haar random unitaries. We can therefore adopt the depolarizing channel as our fundamental noise model. Two two extreme scenarios of depolarizing noises can be employed to approximate the QV random-circuit sampling, which are visualized in Figure 6. In the case of strong cross-talk between qubits, the global depolarizing noise applies, in which the depolarizing channel impacts

all qubits together (see Section III A). In the other situation where cross-talk among qubits is negligible, the single-qubit depolarizing noise is applicable (see Section III B). For the single-qubit depolarizing noise, the depolarizing channel affects each qubit individually. In the QV benchmarking, which necessitates the random permutation of qubits, these two approximations are shown to be equivalent in Section III B.

With these error models, one can evaluate the benchmarking of QV random-circuit sampling employing either the average gate fidelity, heavy output probability, or linear cross-entropy as the figure of merit. Under the single-qubit error model, we show the one-to-one correspondence of these three metrics in the QV random-circuit sampling. Such a correspondence enables us to treat heavy output probability and linear cross-entropy as the function of the average gate fidelity, which benefits us in two folds. Namely, it provides us an analytical tool for studying HOP and LXE through the calculation of AGF, as well as the potential to estimate the AVG from experimental data of HOP or LXE.

A. Global depolarizing noise

In the vectorization representation, the effect of the N -qubits depolarizing channel acting on N -qubits state $|\rho\rangle\rangle$ is

$$\tilde{D}_P^{(N)}|\rho\rangle\rangle = P|\rho\rangle\rangle + \frac{(1-P)}{2^N}|\mathbb{I}_{2^N}\rangle\rangle, \quad (11)$$

where we call P the preserving factor of the depolarizing channel. For $P = 1$, one has perfect identity operator, while for $P = 0$, one obtains a complete depolarizing channel. As shown in Fig. 6 (a), the quantum circuit implementation of $U = u_N \cdots u_1$ under the global depolarizing noise is then given as follows,

$$\begin{aligned} \tilde{U} &= \tilde{u}_N \cdots \tilde{u}_2 \tilde{u}_1 \\ &= \tilde{D}_{P_N}^{(N)} \cdot \hat{u}_N \cdots \tilde{D}_{P_2}^{(N)} \cdot \hat{u}_2 \cdot \tilde{D}_{P_1}^{(N)} \cdot \hat{u}_1. \end{aligned} \quad (12)$$

Since the global depolarizing channel commutes with all other channels, we can simplify Eq. (12) by moving all depolarizing channels to the end of the circuit and retaining only one depolarizing channel with an effective global preserving factor \wp ,

$$\tilde{U} = \tilde{D}_\wp^{(N)} \cdot \hat{U}, \quad \text{with } \wp = \prod_j P_j. \quad (13)$$

Under this global depolarizing noise approximation, the average gate fidelity for a given random circuit U can be then expressed a function of the effective preserving factor,

$$\begin{aligned} F_U(\wp) &= \int_{\Psi} d\psi \langle\langle \psi | \hat{U}^\dagger \tilde{D}_\wp^{(N)} \hat{U} | \psi \rangle\rangle \\ &= \wp + \frac{1}{2^N}(1 - \wp). \end{aligned} \quad (14)$$

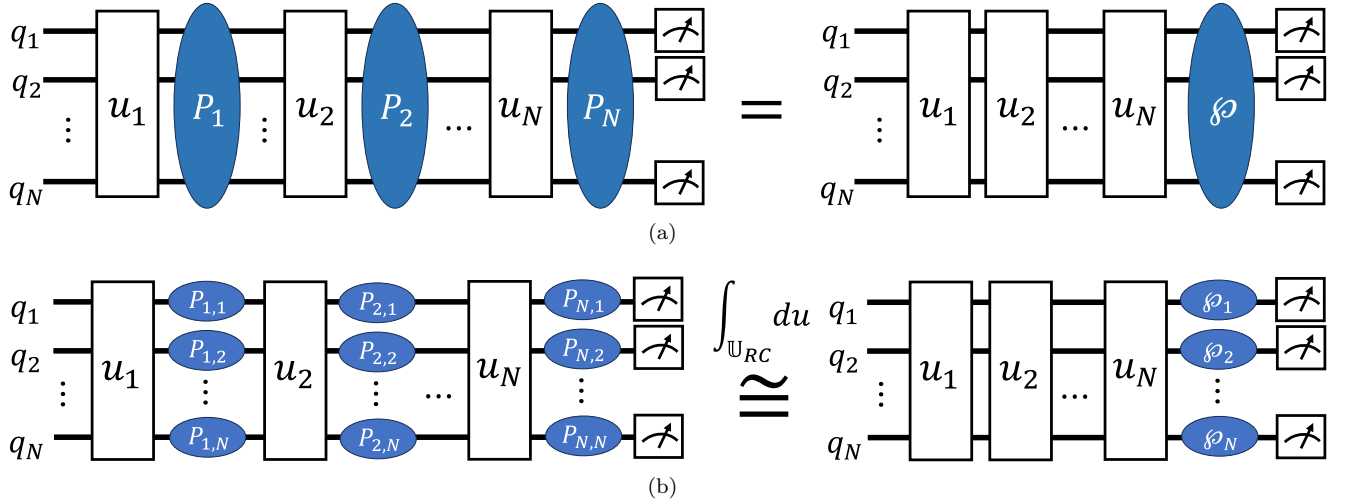


FIG. 6. (a) The global depolarizing channel (blue ellipse) coming after every layer of the random gates u_i and acts on all the qubits globally. (b) The single-qubit depolarizing channels (blue ellipse) coming after every layer of the random gates u_i and acts on each qubit individually.

Similarly, we can determine the HOP as a function of the preserving factor:

$$\begin{aligned} H_U(\varphi) &= \sum_{x \in X_U} \langle \langle x | \tilde{D}_\varphi^{(N)} \hat{U} | 0^N \rangle \rangle \\ &= H_U^{\text{ideal}} \varphi + \frac{1}{2}(1 - \varphi). \end{aligned} \quad (15)$$

Here, H_U^{ideal} is the ideal HOP for the circuit U , and the X_U is the set of heavy outputs of U . Regarding the linear cross-entropy, we can write it as

$$\begin{aligned} \chi_U &= 2^N \sum_x \langle \langle x | \tilde{D}_\varphi^{(N)} \hat{U} | 0^N \rangle \rangle \langle \langle x | \hat{U} | 0^N \rangle \rangle - 1 \\ &= \chi_U^{\text{ideal}} \varphi. \end{aligned} \quad (16)$$

Although this approximation seems rough, later analysis reveals its effectiveness in illuminating the relationship between average gate fidelity, HOP, and linear cross-entropy.

B. Single-qubit depolarizing noise

In the single-qubit error approximation, we apply two single-qubit depolarizing channels after each two-qubit gate. As shown in Fig. 6 (b), in the vectorization presentation, the quantum channel of a random circuit under single-qubit depolarizing noises can be written as

$$\tilde{U} = \tilde{D}_{\vec{P}_N} \cdot \hat{u}_N \cdot \dots \cdot \tilde{D}_{\vec{P}_2} \cdot \hat{u}_2 \cdot \tilde{D}_{\vec{P}_1} \cdot \hat{u}_1, \quad (17)$$

where $\tilde{D}_{\vec{P}}$ is the tensor product of the single qubit depolarizing channels and $\vec{P} = (P_{q_1}, P_{q_2}, \dots, P_{q_N})$ is a vector, whose q component P_q is the preserving factor of the single-qubit depolarizing channel acting on the qubit q ,

$$\tilde{D}_{\vec{P}} \equiv \bigotimes_{q \in \mathbb{Q}} \tilde{D}_{P_q}^{(1)}. \quad (18)$$

Here, the $\mathbb{Q} = \{q_1, q_2, \dots, q_N\}$ is the set of qubits of a QPU.

Unlike the global depolarizing channel, the single-qubit depolarizing channel typically does not commute with other channels. However, in the present scenario, our unitary operators are sampled randomly from the Haar uniform distribution. Such a random sampling allow us to make an assumption that $\tilde{D}_{\vec{P}} \cdot \hat{u} = \hat{u} \cdot \tilde{D}_{\vec{P}}$ holds for all unitary channels. We arrived at this assumption by considering the behavior of a random $\text{SU}(4)$ gate generated according to the Haar uniform distribution in relation to the single-qubit depolarizing channel. Specifically, we observed that, on average, the random $\text{SU}(4)$ gate commutes with the single-qubit depolarizing channel. Mathematically, this can be expressed as

$$\int_{U \in \text{SU}(4)} dU [\hat{U}, \hat{\mathbb{I}} \otimes \tilde{D}_P^{(1)}] = 0, \quad \forall P \in [0, 1]. \quad (19)$$

A detailed proof of this commutation relation is provided in Appendix A. In this single-qubit depolarizing-noise model, our channel only contains two-qubit gates and single-qubit depolarizing channels. We can therefore rearrange the order of operations by moving all depolarizing channels to the end of the circuit,

$$\tilde{U} = \tilde{D}_{\vec{P}} \cdot \hat{U} \quad (20)$$

Note that this effects of noises are independent of the circuit. The the measurement statistics $p_U(n)$ under the single-qubit depolarizing noise model is then given by

$$p_U(n) \equiv \langle \langle n | \tilde{D}_{\vec{P}} \cdot \hat{U} | 0^N \rangle \rangle, \quad (21)$$

which can be formulated as a Markov chain acting on the

ideal outcome distribution.

$$\begin{aligned} p_U(n) &= \sum_{m \in \{0,1\}^N} \langle \langle n | \tilde{D}_{\vec{P}} | m \rangle \rangle \langle \langle m | \hat{U} | 0^N \rangle \rangle \\ &= \sum_{m \in \{0,1\}^N} D_{\vec{P}}(n|m) q_U(m). \end{aligned} \quad (22)$$

Here, $q_U(m) = \langle \langle m | \hat{U} | 0^N \rangle \rangle$ is the ideal probability. The probability vector $\mathbf{p}_U \equiv \{p_U(n)\}_n$ is therefore obtained from the Markov matrix of the transfer probability $D_{\vec{P}}(n|m)$:

$$\begin{aligned} D_{\vec{P}} &\equiv \{D_{\vec{P}}(n|m)\}_{n,m} \\ &= \bigotimes_{q \in \mathbb{Q}} \left(P_q \begin{bmatrix} 1 & 0 \\ 0 & 1 \end{bmatrix} + \frac{1-P_q}{2} \begin{bmatrix} 1 & 1 \\ 1 & 1 \end{bmatrix} \right) \end{aligned} \quad (23)$$

In this formulation, the average gate fidelity is the diagonal element of the Markov matrix,

$$\begin{aligned} F_U(\vec{P}) &= \int_{\Psi} d\psi \langle \langle \psi | \hat{U}^\dagger \tilde{D}_{\vec{P}} \hat{U} | \psi \rangle \rangle = \langle \langle 0^N | \tilde{D}_{\vec{P}} | 0^N \rangle \rangle \\ &= \prod_{q \in \mathbb{Q}} \frac{1+P_q}{2}. \end{aligned} \quad (24)$$

Note that the average gate fidelity is independent of U , hence we obtain the average AGF $\bar{F} = F_U(\vec{P})$. It can be also expressed by an effective global preserving factor \wp

$$\bar{F} = \wp + \frac{1}{2^N} (1 - \wp), \quad \wp \equiv \frac{\prod_{q \in \mathbb{Q}} (1+P_q)^2 - 1}{2^N - 1} \quad (25)$$

The determination of the vector of effective preserving factor $\vec{P} = (P_{q_1}, \dots, P_{q_N})$ will be discussed in the next section.

To calculate the heavy output probability, we first express it as the inner product between the probability vector and the heavy output vector \mathbf{h}^U .

$$H_{ideal}^U = \sum_{n \in \{0,1\}^N} h_n^U p_U(n) \quad (26)$$

$$h_n^U = \begin{cases} 1 & \text{if } n \in X_U \\ 0 & \text{if } n \notin X_U \end{cases} \quad (27)$$

We then define the average probability vector $\bar{\mathbf{p}}$ by rearranging the probability vector in descending order.

$$\bar{\mathbf{p}} = \int_U dU \Pi_U \mathbf{p}_U \quad (28)$$

The average HOP is then obtained by summing the probabilities of the top half of the average probability vector $\bar{\mathbf{h}} = \{\bar{h}_n\}_n$, and replace the binary index n with decimal index.

$$\begin{aligned} \bar{H}_{ideal} &= \sum_n \bar{h}_n \bar{p}_n \\ \text{with } \bar{h}_n &= \begin{cases} 1 & \text{if } n < 2^{N-1} \\ 0 & \text{if } n \geq 2^{N-1} \end{cases} \end{aligned} \quad (29)$$

Although predicting the set of heavy outputs X_U for different U is generally challenging, the random circuit's structure offers insights. With uniform random permutations among qubits and $SU(4)$ gates under the Haar measure, the probability of obtaining a specific heavy output remains constant. Therefore, we can approximate the average heavy output probability, accounting for errors, by utilizing the Markov matrix outlined in Eq. (22), considering the average over all permutations,

$$\begin{aligned} \bar{H}(\vec{P}) &= \frac{1}{2^N!} \sum_{\Pi \in \mathbf{S}_{2^N}} \bar{\mathbf{h}}^T \cdot \Pi^T D(\vec{P}) \Pi \cdot \bar{\mathbf{p}}, \\ &\equiv \bar{\mathbf{h}}^T \cdot \bar{D}(\vec{P}) \cdot \bar{\mathbf{p}}, \end{aligned} \quad (30)$$

where Π is the permutation matrix and \mathbf{S}_{2^N} is the permutation group. After averaging over permutations, one obtains an effective Markov matrix $\bar{D}(\vec{P})$,

$$\bar{D}(\vec{P}) \equiv \sum_{\Pi \in \mathbf{S}_{2^N}} \Pi^T D(\vec{P}) \Pi. \quad (31)$$

The diagonal element of $\bar{D}(\vec{P})$ is the average of all diagonal elements of $D(\vec{P})$, while the off-diagonal elements of $\bar{D}(\vec{P})$ is the average of all off-diagonal elements of $D(\vec{P})$. The diagonal elements in $\bar{D}(\vec{P})$ is therefore equal to \bar{F} . Since $\bar{D}(\vec{P})$ is a symmetric Markov matrix, we deduce that all off-diagonal elements are equal to $\frac{1-\bar{F}}{2^N-1}$.

$$\begin{aligned} \bar{D}(\vec{P}) &= \frac{1}{2^N!} \sum_{\Pi \in \mathbf{S}_{2^N}} \Pi^T D(\vec{P}) \Pi \\ &= \begin{bmatrix} \bar{F} & \frac{1-\bar{F}}{2^N-1} & \cdots & \frac{1-\bar{F}}{2^N-1} \\ \frac{1-\bar{F}}{2^N-1} & \bar{F} & \cdots & \frac{1-\bar{F}}{2^N-1} \\ \vdots & \vdots & \ddots & \vdots \\ \frac{1-\bar{F}}{2^N-1} & \frac{1-\bar{F}}{2^N-1} & \cdots & \bar{F} \end{bmatrix}. \end{aligned} \quad (32)$$

From Eq. (32), one can see that $\bar{D}(\vec{P})$ is a Markov matrix under the global depolarizing-noise model, which implies that averaging over permutations leads us back to the global depolarizing approximation.

Consequently, we arrive at the average HOP \bar{H} as a functions of the average AGF \bar{F} , which are then given by the effective global preserving factor \wp ,

$$\begin{aligned} \bar{H}(\vec{P}) &= \bar{H}_{ideal} \frac{2^N \bar{F} - 1}{2^N - 1} + (1 - \bar{F}) \frac{2^{N-1}}{2^N - 1} \\ &= \bar{H}_{ideal} \wp + \frac{1}{2} (1 - \wp) \end{aligned} \quad (33)$$

The same result holds for and the LXE

$$\bar{\chi}(\vec{P}) = \frac{2^N \bar{F} - 1}{2^N - 1} \bar{\chi}_{ideal} = \bar{\chi}_{ideal} \wp \quad (34)$$

A linear relation between linear cross-entropy benchmarking and heavy output testing can be then derived,

$$\bar{H}(\vec{P}) = \frac{1}{2} + \frac{1}{2} \ln 2 \frac{\bar{\chi}(\vec{P})}{\bar{\chi}_{ideal}}. \quad (35)$$

This two equations implies the one-to-one correspondence among average HOP, LXE and average AGF. This one-to-one correspondence is exact the same as the their relation in global depolarizing-noise model. It implies the equivalence between global depolarizing noise and single-qubit depolarizing noise in the random-circuit benchmarking. In the large size limit ($2^N \gg 1$), this one-to-one correspondence can be simplified to

$$\bar{H}(\vec{P}) \approx \frac{1 + \bar{F} \ln 2}{2}, \quad \bar{\chi}(\vec{P}) \approx \bar{F} \bar{\chi}_{ideal}. \quad (36)$$

In the quantum volume benchmarking, if devices pass the test, then we must have $\bar{H}(\vec{P}) > \frac{2}{3}$. So the threshold for the linear cross-entropy, by the suggestion of the quantum volume benchmarking, is $\bar{\chi}(\vec{P}) > \frac{1}{3 \ln 2} \bar{\chi}_{ideal}$, and similar for the average gate fidelity. Another important consequence of Eq. (33) and Eq. (34) is that now HOP and LXE are the linear functions of the average gate fidelity for arbitrary two QPUs with \vec{P}_Q and $\vec{P}_{Q'}$, we had:

$$\begin{aligned} \bar{F}(\vec{P}_Q) \geq \bar{F}(\vec{P}_{Q'}) &\Leftrightarrow \bar{H}(\vec{P}_Q) \geq \bar{H}(\vec{P}_{Q'}) \\ &\Leftrightarrow \bar{\chi}(\vec{P}_Q) \geq \bar{\chi}(\vec{P}_{Q'}) \end{aligned} \quad (37)$$

As a result of Eq. (37), we only need to employ average gate fidelity to evaluate the performance of QPUs, which is our main focus in the next section.

C. The error model for DQC under connectivity constraints

In the previous section, we derive a one-to-one correspondence relation among different metrics QV random-circuit benchmarking, which allows us to employ average AGF to evaluate quantum computing device. According Eq. (24) and (25), the average AGF is determined by the effective preserving factors $\vec{P} = (P_{q_1}, \dots, P_{q_N})$. In this section, we will establish a theory for determining the vector \vec{P} under connectivity constraints.

We start our analysis with the fully connected single-QPU device, which is the simplest case. An N -qubit quantum volume circuit has N layers of gates. In each layer, there are $\lfloor \frac{N}{2} \rfloor$ SU(4) gates acting on N qubits. In the single-qubit depolarizing noise model, each SU(4) gate is followed by two single-qubit depolarizing channels. There are in total $2N \lfloor \frac{N}{2} \rfloor$ depolarizing channels acting on the N qubits. Here, we assume the preserving factor P_q of a single-qubit depolarizing channel is a constant for a qubit q , independent of layers. The average gate fidelity can be then estimated by the following formula,

$$\bar{F} = \prod_{q \in \mathbb{Q}} \frac{1 + P_q^{2 \lfloor \frac{N}{2} \rfloor}}{2}, \quad (38)$$

where the \mathbb{Q} is the set of qubits representing a QPU.

For a QPU with limited connectivity, additional swapping gates are needed. For multi-QPU DQC, one needs auxiliary qubits for telegating. Both processes introduce additional noises to the implementation of quantum computing. To assess the average AGF of multi-QPU DQC with limited connectivity one needs to incorporate the noises introduced by swapping gates and the telegating processes into the effective preserving factors \vec{P}_q . We achieve this by introducing an allocation matrix $\{A_{q,q'}\}_{q,q' \in \mathbb{Q}}$ modeled with the single-qubit depolarizing noises. Each element $A_{q,q'}$ of the allocation matrix describes the average number of single-qubit depolarizing channels propagating from the qubit q' to the qubit q , when one implements a random two-qubit SU(4) gate on q . The effective preserving factor \vec{P}_q for a qubit q in multi-QPU DQC is therefore given by

$$\vec{P}_q = \prod_{q' \in \mathbb{Q}} P_{q'}^{A_{q,q'}}, \quad (39)$$

where \mathbb{Q} is the set of all qubits on the composited QPUs. For example, in the DQC device represented by the extended connectivity graphs shown in Fig. 7 (b) and (c), the complete qubit set $\mathbb{Q} = \mathbb{Q}_w \cup \mathbb{Q}_m$ includes the set of working qubits $\mathbb{Q}_w = \{q_1, \dots, q_8\}$ and the set of memory qubits $\mathbb{Q}_m = \{m_A, m_B\}$. Note that, the preserving parameter P_q quantifies the quality of a direct two-qubit gate acting on two connected qubits, while the allocation matrix $A_{q,q'}$ characterizes the connectivity topology and the memory allocation of a multi-QPU DQC device, which are represented by an extended connectivity graph. Since the benchmarking only evaluates the measurement readouts of the working qubits, the average AGF is solely determined by the effective preserving factors \vec{P}_q of the working qubits $q \in \mathbb{Q}_w$. One therefore arrives at the following formula for the average AGF in a multi-QPU DQC device,

$$\bar{F} = \prod_{q \in \mathbb{Q}_w} \frac{1 + \vec{P}_q^{2 \lfloor \frac{N}{2} \rfloor}}{2}. \quad (40)$$

To determine the allocation matrix for a given extended connectivity graph, we analyze the implementation cost of a random two-qubit gate between two qubits q and q' . The cost that one needs to pay is the single-qubit depolarizing channels introduced by additional swapping gates under limited connectivity of \mathbb{Q}_w and telegating across the auxiliary qubits \mathbb{Q}_m . For the example shown in Fig. 8, in the n -th layer of a QV random-circuit benchmarking, one randomly chooses a two-qubit unitary u_n acting on the qubits $\{q_1, q_3\}$, as shown in Fig. 8 (b). Under the extended connectivity of the two-QPU DQC device shown in Fig. 8 (a), the implementation of u_n introduces depolarizing channels, which are depicted as the circles in Fig. 8 (c). Taking the average over the QV random-circuit sampling, the one can approximately moving all single-qubit depolarizing channels to the end

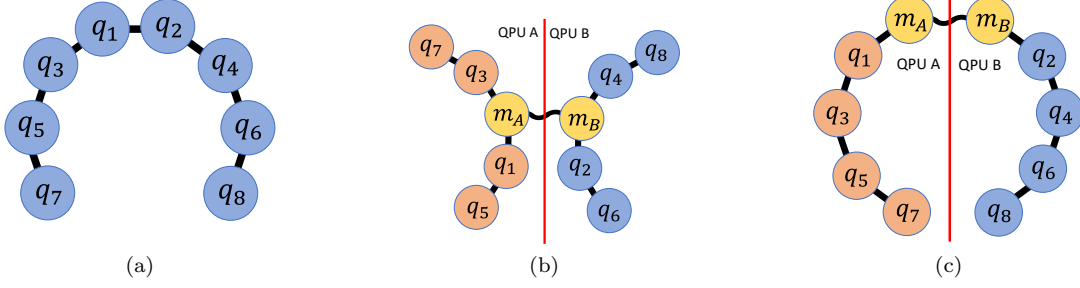


FIG. 7. Extended connectivity graph. The distinction between graphs (b) and (c) is the positioning of the auxiliary memory qubits. Notably, the graphs (a) and (c) coincide if the auxiliary memory qubits are replaced with a coupling between q_1 and q_2 . (a) A 1D connectivity graph of a single QPU with 8 qubits. (b) A two-1D-QPU DQC connectivity graph with 8 working qubits in total. The memory qubit on each QPU stores an entangled pair between the two QPUs. (c) A two-1D-QPU DQC connectivity graph resulting a new extended 1D connectivity graph.

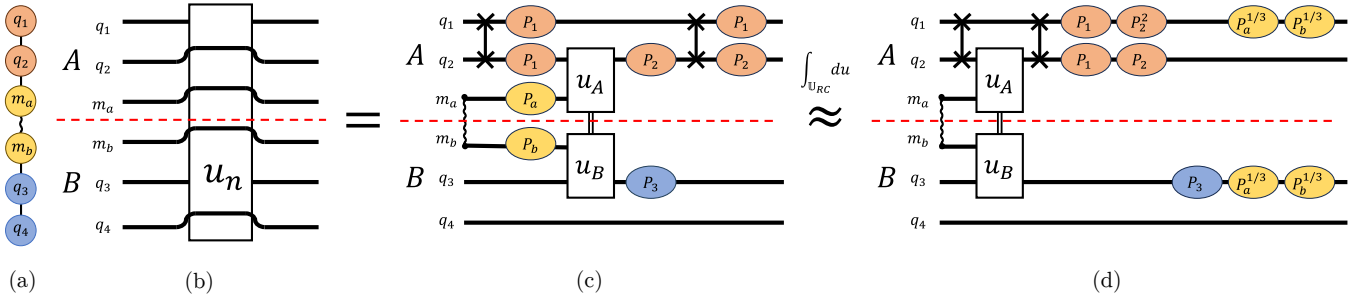


FIG. 8. From extended connectivity graph to cost matrices. (a) An extended connectivity graph with the working qubits $\mathbb{Q}_w = \{q_1, q_2, q_3, q_4\}$ and the memory auxiliary qubits $\mathbb{Q}_m = \{m_a, m_b\}$. (b) A random two-qubit gate u_n acts on the qubit $\{q_1, q_2\}$. (c) An implementation of u_n with single-qubit depolarizing noises. (d) Moving all single-qubit depolarizing noises to the end of the circuit.

of circuit with the effective preserving factors shown in Fig. 8 (d). For the implementation of u_n on $\{q_1, q_3\}$ under the extended connectivity graph, one can a cost matrix $C(q_1, q_3)$ as follows,

$$C(q_1, q_3) = \begin{bmatrix} 1 & 2 & 0 & 0 & \frac{1}{3} & \frac{1}{3} \\ 1 & 1 & 0 & 0 & 0 & 0 \\ 0 & 0 & 1 & 0 & \frac{1}{3} & \frac{1}{3} \\ 0 & 0 & 0 & 0 & 0 & 0 \end{bmatrix}. \quad (41)$$

Each element $C_{n,m}(q_1, q_3)$ of the cost matrix counts the number of depolarizing channels originated from the qubit q_m and acting on the working qubit q_n . Note that a cost matrix $C(q, q')$ contain N rows of working qubits and $N + M$ columns of working and auxiliary memory qubits. The detailed steps and examples of calculating this cost matrix are provided in Appendix B.

Finally, we define the allocation matrix A by aggregating the cost matrices of all pairs of working qubits,

$$A \equiv \frac{1}{2(N-1)} \sum_{q, q' \in \mathbb{Q}_w} C(q, q') \quad (42)$$

Here, the cost matrices are divided by $2(N-1)$ to ensure that the allocation matrix of a fully connected QPU is

normalized to $A_{q,q'} = \delta_{q,q'}$, such that Eq. (38) aligns with Eq. (40) as a special case.

IV. NUMERICAL SIMULATION OF BENCHMARKING

In this section, we employ numerical simulation to scrutinize the one-to-one correspondence among HOP, LXE, and AGF in our single-qubit depolarizing approximation outlined in the preceding section. We adopt the average AGF as the figure of merit for the two-QPU DQC benchmarking, and show a performance improvement of DQC under limited connectivity, which indicates the enhancement of scalability of quantum computing through DQC.

We employ the same random circuit structure utilized in quantum volume benchmarking to compute both the HOP and linear cross-entropy. However, it should be noted that the specific random circuit structure chosen should not undermine our results, given that they all effectively approximate the Haar uniform unitaries. To reduce the total number of gates and the efficiency of the circuit compiling, we replace the permutation gates

in QV random circuits by repositioning the $SU(4)$ gates. The $SU(4)$ gates are samples through the KAK decomposition, in which any $SU(4)$ gate can be expressed as a sequence of single-qubit operations and three CNOT gates.

For global $SU(4)$ gates acting across the two local QPUs, we apply the EJPP protocol to these CNOT gates. We then can implement all the non-local $SU(4)$ gates through DQC, as depicted in Fig. 9. It is worth noting that this approach necessitates three entangled pairs to implement a single $SU(4)$ gate. Alternatively, utilizing quantum state teleportation reduces this requirement to two entangled pairs (one for sending the state and one for returning it). However, adopting quantum state teleportation entails the addition of one more qubit to each local QPU. The utility of the EJPP delegating protocol minimizes the number of auxiliary memory qubits to one within each local QPU, and hence maximize the number of working qubits.

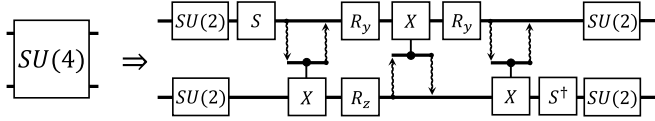


FIG. 9. Implementation of a non-local $SU(4)$ gate using the EJPP protocol. The diagram illustrates the application of three independent EJPP protocols to realize the $SU(4)$ gate via DQC.

In our simulation, we select six types of connectivity, which can be categorized into two groups. The first group comprises devices utilizing a single QPU, while the second group consists of DQC-composited devices equipped with two local QPUs. Within each group, the local QPUs exhibit three types of connectivity graphs, namely fully connected graph, 1D (line) graph, and 2D (grid) graph, respectively. Fig. 10 illustrates the extended connectivity graphs of our simulation devices. Solid lines denote the coupling between physical qubits, while wavy lines represent the sharing of entangled pairs between auxiliary memory qubits. For the two-QPU DQC devices, each local QPU contains only one auxiliary memory qubit. The allocation of the auxiliary memory qubit is chosen as the hub qubit, which improves the connectivity to the greatest extent. [Explain, fix topology for local QPUs]

We employ qiskit to simulate the QV random benchmarking under the single-qubit depolarizing noise model. With Eq. (34), we employ linear cross-entropy for measuring average gate fidelity. The simulation is conducted as follows. In the first run, we set a constant error rate $\epsilon = 0.05\%$ ($\epsilon \equiv 1 - P$) across all qubits in qiskit, and conduct QV random-circuit sampling on different types of connectivity for n -qubit devices, where $n = 5, \dots, 8$. For simplicity, we assumed that all entangled pairs were perfect. In the next runs, we vary the error rates ϵ from 0.05% to 0.5% and implement the same QV random-circuit sampling. We sampled over 1000 random circuits for each connectivity graph and error rate, and executed

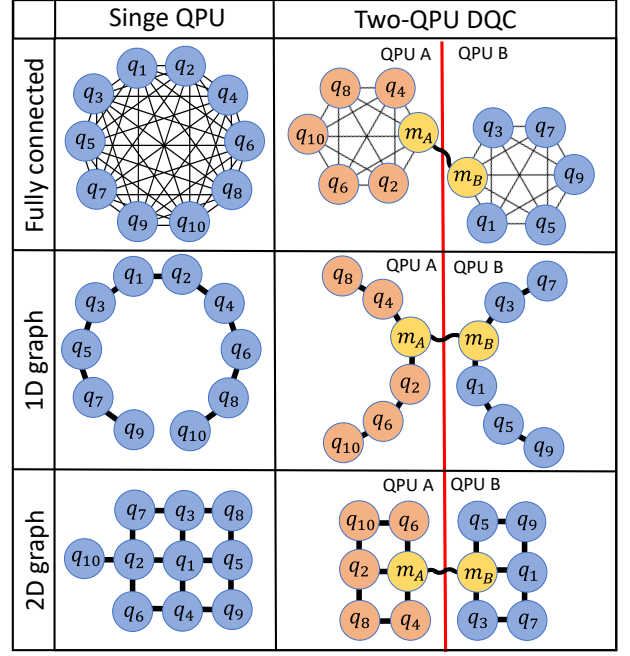


FIG. 10. Extended connectivity graphs for simulation. The first column is the group of single-QPU devices, where the blue vertices represent the working qubits that are responsible for the computing, and the black edges identify the direct coupling between qubits. The second column is the group of two-QPU DQC devices, where the blue and orange vertices represent the working qubits of the local QPUs, and the yellow vertices denote the auxiliary memory qubits. Each auxiliary memory qubit can either store the shared entangled state or facilitate the passage of additional swapping gates.

10,000 shots for each sampled circuit. After the sampling, for each connectivity graph and error rate, we obtain an average AGF \bar{F} , which are plotted by different markers in Fig. 11 (a,c,e,g).

To verify the result in Eq. (40), we calculate the effective preserving factor P_{eff} , as well as the effective error rate $\epsilon_{\text{eff}} \equiv 1 - P_{\text{eff}}$ from each average AGF data according to Eq. (40). In Fig. 11 (b,d,f,h), the effective error rates ϵ_{eff} are compared with the initial inputs ϵ_{in} of the qiskit function. From the simulation, we observe that the effective error rates are linearly proportional to the input error rates with a ratio $r_{G,n}$ around $0.8 \sim 1$ varying with different types of connectivity G and qubit numbers n ,

$$\epsilon_{\text{eff}} = r_{G,n} \epsilon_{\text{in}}. \quad (43)$$

Ideally, one expects $r_{G,n} = 1$, however, a small distinction arises. This discrepancy stems from the difference between our error model and the compilation in qiskit. In our error model, we treat every $SU(4)$ gate as a fundamental building block and assume that all the errors are single-qubit depolarizing noises. On the other hand, in qiskit, an $SU(4)$ gate is decomposed into a sequence of single-qubit gates and CNOT gates, which are subject to single-qubit and two-qubit depolarizing channels, respec-

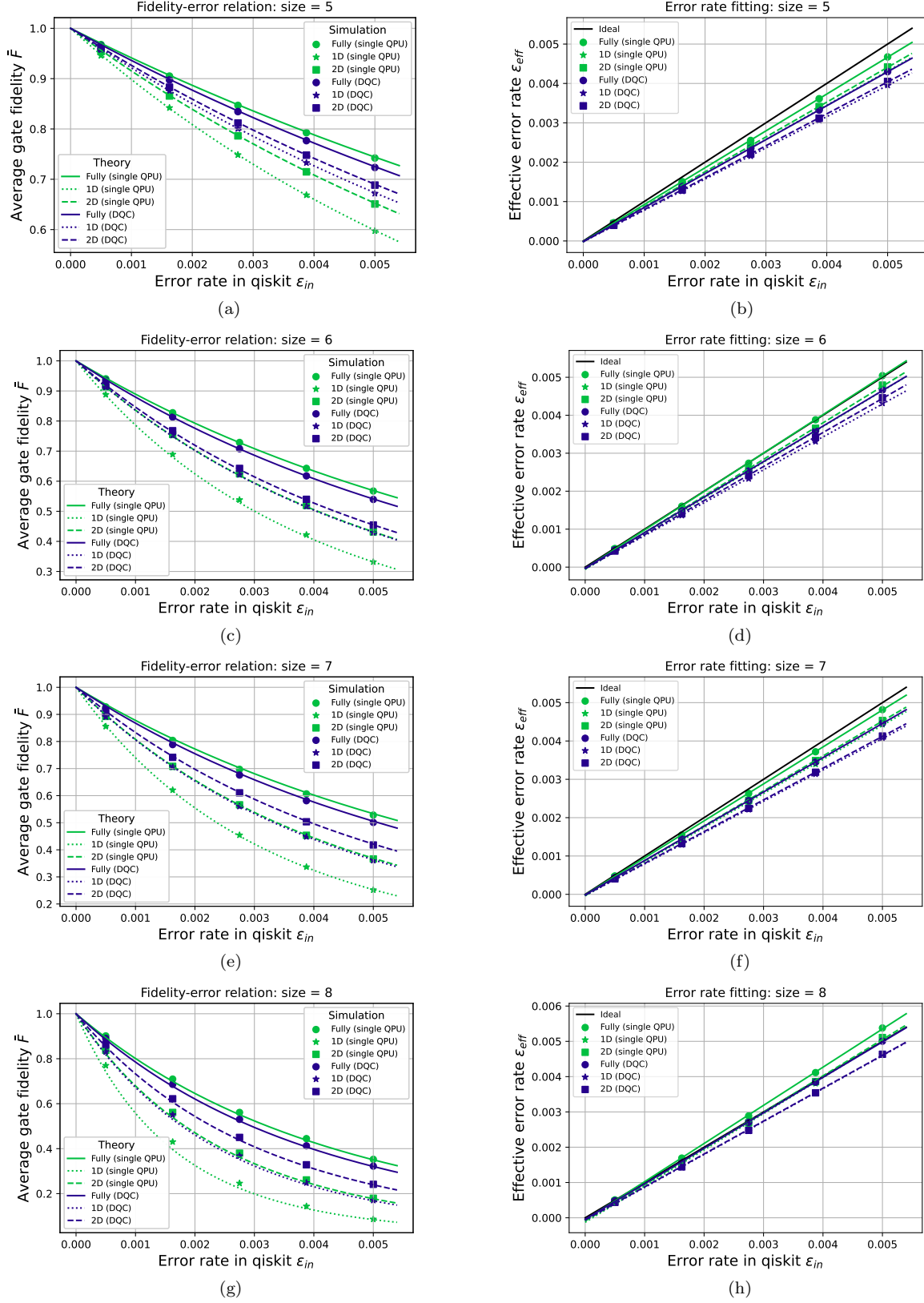


FIG. 11. (a),(c),(e),(g) Average gate fidelity of 5-qubit devices with different types of connectivity. The data points represent the average gate fidelity obtained from numerical simulation for different error rates. The lines show the theoretical prediction of average gate fidelity derived from Eq. (40). (b),(d),(f),(h) Comparison between the error rate specified in the qiskit noise model and the error rate estimated through our average gate fidelity formula in Eq. (40). The markers represent the data points obtained from our simulation, while the lines represent the linear fitting of our data.

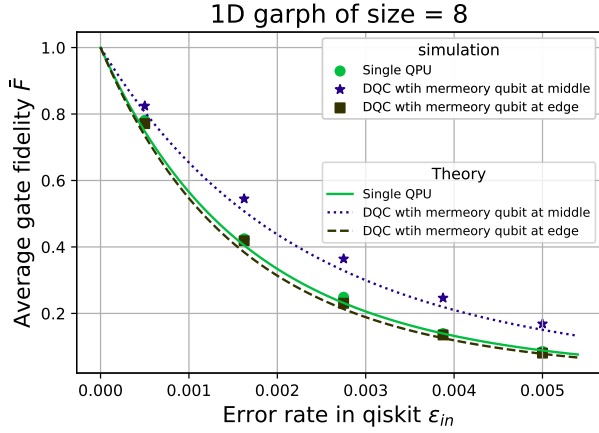


FIG. 12. Average AGF of 1D connectivity graph shown in Fig. 7 for different error rates. The two-QPU DQC device in Fig. 7(b) featuring memory qubits positioned in the middle, which exhibits a significant advantage over the single-QPU device. However, the two-QPU DQC device with memory qubits at the edges does not offer any advantage. Therefore, the strategic selection of the auxiliary memory qubit’s positions on each local QPU emerges as a critical condition for scalability enhancement.

tively. [The strong linearity between ϵ_{eff} and ϵ_{in} provides a compelling evidence for the validity of Eq. (40).]

Due to the lack of knowledge about the detailed compilation in qiskit, we should use the ratio $r_{G,n}$ fitted in Fig. 11 (b,d,f,h) to calibrate the effective preserving factor from Eq. (39),

$$\bar{P}_q = \prod_{q' \in \mathbb{Q}} (1 - r_{G,n} + r_{G,n} P_{\text{in}})^{A_{q,q'}}. \quad (44)$$

Employing this calibrated effective preserving factor, we plot the theoretical prediction of Eq. (40) for different connectivities by lines in Fig. 11 (a,c,e,g). One can observe that the theoretical predictions in Eq. (40) and the simulate results evaluated through the AGF-HOP correspondence in Eq. (33), align with each other very well. It verifies both the AGF-HOP correspondence in Eq. (33) and our error model in Eq. (40).

Besides, in Fig. 11 (a,c,e,g), one can also observe that single fully connected QPU exhibits the highest average gate fidelity among the different connectivity graphs, which is expected as there are no additional gates introduced. Its corresponding two-QPU DQC devices perform slightly worse, as additional gates for telegating applied. On the contrary, for 1D and 2D connectivity, the two-QPU DQC devices outperform the single-QPU device for all n -qubit devices, which show the enhancement of scalability in two-QPU DQC under limited connectivity. The condition for such scalability enhancement depends on the connectivity of QPUs. To confirm this assertion, we conduct another simulation for 1D connectivity, where we relocate the auxiliary memory qubit in each QPU to the end of the line graph, as illustrated in Fig. 7 (c). In

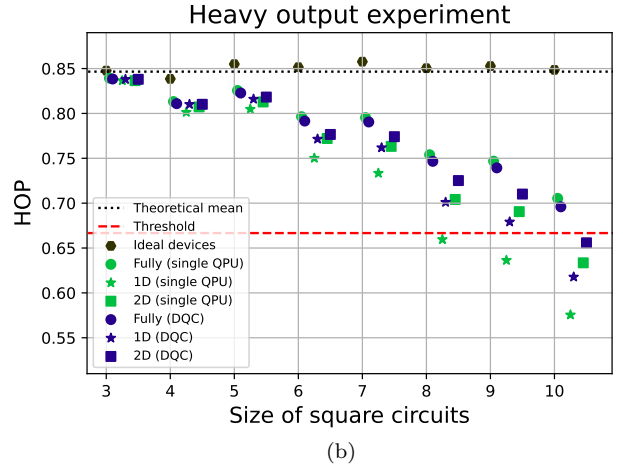
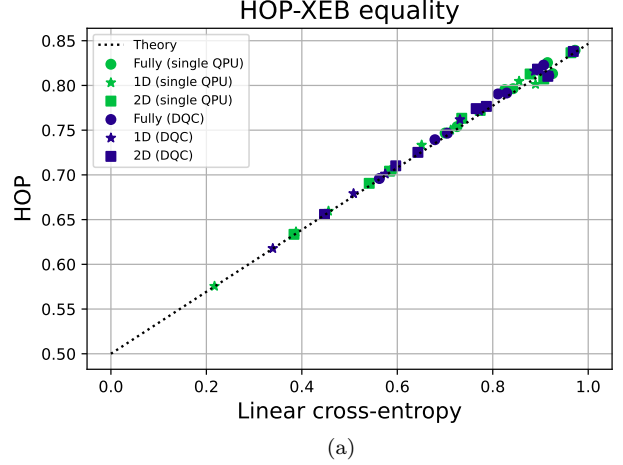


FIG. 13. QV random-circuit benchmarking for n -qubit devices with different types of connectivity. Here the size of devices ranges from 3 to 10. (a) HOP-LXE correspondence. (b) HOP for different sizes and connectivity.

this configuration, the two-QPU DQC device resembles a single-QPU device with a line graph topology. Since the implementation of DQC does not enhance the connectivity, and meanwhile there will be additional error costs introduced by telegating, we expect no scalability enhancement for this configuration, which aligns with the simulation results plotted in Fig. 12.

To further support the AGF-HOP-LXE correspondence and scalability enhancement of DQC, we conduct additional simulations, in which we fix the error rate $\epsilon_{\text{in}} = 0.15\%$ for all qubits, and benchmark both single-QPU and two-QPU devices from 3-qubit to 10-qubit. Under this setting, we sample over 2000 random circuits for all sizes and take 10000 shots for each random circuit. For each configuration of connectivity graph G and qubit number n , we evaluate the measurement outputs with both average HOP and LXE, and plot them in Fig. 13(a).

One can clearly verify the HOP-LXE correspondence derived in Eq. (35) with these simulated data as a general property independent of device size and connectivity.

Employing the obtained data, we evaluate the quantum volume of different devices in Fig. 13(b), which offer insights into the scalability of device architecture by illustrating how the HOP decreases with increasing device size. It shows that, for a fully connected QPU, the DQC configuration doesn't offer advantage over a single-QPU setup. Note that this statement is only made for the situation when the error rates of multiple small-size QPUs are the same as the error rate of a large-size single QPU. However, in practice, the error rate of a small-size QPU is usual smaller than the one of a large-size QPU.

Besides the fully connectivity, for the devices with 1D and 2D connectivity graphs, we observe that the two-QPU DQC devices exhibits superior HOP compared to the single-QPU configuration. Especially for 1D connectivity, we observe the increase of quantum volume from 2^7 to 2^9 through DQC. These observations suggest that the connectivity of the devices plays a pivotal role in the scalability analysis of multi-QPU DQC under the QV random-circuit benchmarking scheme.

V. RESULTS AND DISCUSSION

Our theoretical calculation and numerical simulation of QV random-circuit benchmarking show that the scalability enhancement in DQC strongly depends on the connectivity of QPUs, the choice of the auxiliary memory qubits for establishing a quantum communication channel, and the quality of entanglement distribution.

First, for fully connected devices shown in Fig. 11 and Fig. 13 (b), DQC does not improve the scaling of quantum computing, if the error rate of a QPU of a larger size is the same as a smaller-size QPU. The underlying reason is the additional gates in the EJPP protocol that cause additional gate errors and lower the circuit's average gate fidelity.

$$\bar{F}_{\text{DQC}}^{\text{fully connected}} < \bar{F}_{\text{single}}. \quad (45)$$

Under the same reason, a more general observation is that the multi-QPU DQC configurations that preserve the topology of single QPUs should not have advantage over single-QPU device, if we assume the same error rate of quantum gates on each QPU regardless of their size in qubit numbers. However, in practice, the gate error rate on a single QPU should increase as the number of qubits increases. Under this consideration, the utility of DQC with small-size QPUs, which have a lower error rate, can also enhance the scalability. For example, according to benchmarking data is plotted in Fig. 12, for the configuration shown in Fig. 8 (c), if the error rate of two 5-qubit QPUs is $\epsilon = 0.1\%$, one would expect an average AGF around $\bar{F} = 0.55$, which is greater than the average AGF

$\bar{F} = 0.43$ of the single-QPU device with $\epsilon = 0.15\%$. In this regard, even without changes of connectivity topology, one can still expect scalability enhancement.

Second, for devices with limited connectivity, DQC can change the connectivity and reduce the number of swapping gates utilized for the implementation of two-qubit gates on two non-neighboring qubits. To improve connectivity in the best way, the auxiliary memory qubits for sharing an entangled Bell pair should be chosen as the qubit that has the highest degree of neighboring qubits. Such an enhancement in connectivity can compensate for and even overcome the additional errors introduced by telegating, so that one can enhance quantum computing performance by scaling up the system through multi-QPU DQC, as it is shown in Fig. 11 and Fig. 13 (b).

$$\bar{F}_{\text{DQC}}^{\text{1D or 2D}} > \bar{F}_{\text{single}}. \quad (46)$$

For large-size QPUs with more complicated connectivity graphs, it is not efficient to try all possible choices of auxiliary memory qubit to find the best DQC configuration for scalability enhancement employing Eq. (40). To provide an efficient analytical tool, we introduce further approximation of average AGF for large-size and high-fidelity QPUs,

$$\bar{F}_{\mathbb{Q}}(\epsilon) \approx \exp\left(-\frac{N\mathcal{A}_{\mathbb{Q}}}{2}\epsilon\right), \quad (47)$$

where the error rate for every qubit is a constant ϵ , and the *characteristic cost* $\mathcal{A}_{\mathbb{Q}}$ of a connectivity configuration \mathbb{Q} is the sum of all elements of the allocation matrix $A_{q,q'}$

$$\mathcal{A}_{\mathbb{Q}} \equiv \sum_{q \in \mathbb{Q}_w, q' \in \mathbb{Q}} A_{q,q'}. \quad (48)$$

Here \mathbb{Q}_w is the set of working qubits and \mathbb{Q} is the set of all qubits including auxiliary qubits for telegating (for detailed derivation see Appendix D). Eq. (47) can be employed as a heuristic method for evaluating connectivity configurations of DQC devices. Fig. 17 is the comparison between Eq. (40) and Eq. (47) for different extended connectivity. and it shows that the approximation works well for $\bar{F} \gtrsim 0.6$, which is around the threshold of QV benchmarking. This implies that this approximation is sufficient for evaluating quantum computing performance in QV random-circuit benchmarking. Moreover, we can also use the approximated formula in Eq. (47) to decide the position of the auxiliary memory qubits on local QPU by minimizing the *characteristic cost* $\mathcal{A}_{\mathbb{Q}}$ over all possible allocation.

Third, there is another implicit requirement for scalability enhancement, that is high-quality entangled pairs shared between local auxiliary memory qubits. In previous analysis and simulation, we assume perfect entangled pairs are distributed among QPUs and only the noises of local gates involved in the EJPP processes contribute errors in telegating. However, the fidelity of entangled pairs

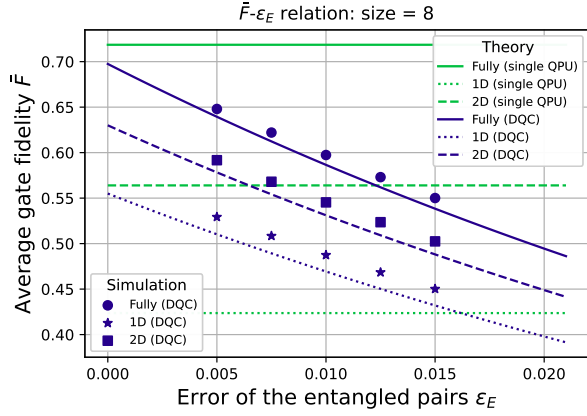


FIG. 14. Robustness of scalability enhancement against the imperfection in entanglement.

strongly affects the capability of delegating for improving the connectivity. If the entanglement is too noisy, delegating will not be capable to enhance the scalability. With a small extension (see Appendix E), the theory of fidelity estimation in Eq. (40) can be employed to analyze the robustness of scalability enhancement in a DQC configuration against the noise ϵ_E in entanglement, where the noise is described as the depolarizing channel with an error rate ϵ_E and a preserving factor $p_E = 1 - \epsilon_E$,

$$D_{p_E}(\Phi) = (1 - \epsilon_E) |\Phi\rangle \langle \Phi| + \epsilon_E \frac{1}{4} \mathbb{I}, \quad (49)$$

and $|\Phi\rangle$ is one of the Bell states. In Fig. 14, we simulate the effect of noise in entanglement on the average gate fidelity and compare them with theoretical prediction. Our theory predicts that the DQC scalability enhancement for 1D and 2D connectivity is robust against the noise ϵ_E up to 0.65% and 1.63%, respectively, which are lower bounds on the simulated results. We can therefore determine the essential requirement on entangled pairs for DQC scalability enhancement employing Eq. (40).

VI. CONCLUSION

In this work, we employ average gate fidelity, heavy output probability, and linear cross-entropy as the figures of merits to benchmark the performance of DQC through random circuit sampling, and compare them with single-QPU quantum computing. Under an approximation using a single-qubit depolarizing error model, we show the one-to-one correspondence among these three figures of merits in Eq. (33), (34), and (35). This relation allows us to obtain a unified evaluation of the performance of quantum computing devices in the random-circuit benchmarking.

The theoretical evaluation according to our theory in Eq. (40) agrees with the simulation results, which show the scalability enhancement in DQC for QPUs with lim-

ited connectivity, such as 1D and 2D graphs shown in Fig. 11 and 13. The results suggest that the condition of scaling up quantum computing using DQC is to choose a good qubit that is connected to a large number of neighbors as the auxiliary memory qubit on each local QPU for the quantum communication channel. And for given local QPUs, we can find the best position for the auxiliary memory qubit, with the help of the allocation matrix A introduced in Eq. (42), and a heuristics method of finding the best position is through the minimization of the characteristic value \mathcal{A}_Q .

In the future, one may generalize the theory in three directions. The first is to consider multipartite DQC-composited devices with more than two local QPUs. The second is to increase the number of auxiliary memory qubits for the quantum communication channel on each local QPU. For example, if there are two auxiliary memory qubits on each local QPU, the DQC-composed device can support the advanced embedding-enhanced distributing processes proposed in [15, 16]. The embedding-enhanced distributing techniques can enhance the efficiency of quantum communication channels and hence improve the average gate fidelity of the delegating implementation. The last is to incorporate qubit allocation in the random circuit benchmarking, which will reduce the number of swapping gates and entangled pairs, and hence improve the quantum computing performance. These three directions are highly related to each other and all play important roles in the development of DQC.

ACKNOWLEDGMENTS

This work is supported by NSTC under the Grant No. 111-2923-M-032-002-MY5, 112-2112-M-032-008-MY3, 112-2811-M-032-005-MY2, 112-2119-M-008-007, and 113-2119-M-008-010.

Appendix A: The commutative hypothesis

In Section IIIB, we proposed a hypothesis asserting the commutativity of the $SU(4)$ gate with the single-qubit depolarizing channel. This hypothesis stems from the observation that, under the Haar measure, a random $SU(4)$ gate tends to commute with the single-qubit depolarizing channel, expressed as:

$$\int_{U \in SU(4)} dU [\hat{U}, \hat{\mathbb{I}} \otimes \tilde{D}_P^{(1)}] = 0 \quad \forall P \in [0, 1] \quad (A1)$$

To substantiate this claim, we draw upon an essential lemma from reference [26], which states that the average unitary transformation under the Haar measure for all linear operators in \mathcal{H}^d is:

$$\int_{U \in SU(d)} dU U X U^\dagger = \frac{\text{tr}(X)}{d} \mathbb{I}_d \quad (A2)$$

By vectorization, we reformulate this lemma as:

$$\int_{U \in SU(d)} dU \hat{U} |X\rangle\rangle = \frac{\text{tr}(X)}{d} |\mathbb{I}_d\rangle\rangle = \frac{1}{d} |\mathbb{I}_d\rangle\rangle \langle\langle \mathbb{I}_d | X \rangle\rangle \quad \forall |X\rangle\rangle \quad (\text{A3})$$

$$\Leftrightarrow \int_{U \in SU(d)} dU \hat{U} = \frac{1}{d} |\mathbb{I}_d\rangle\rangle \langle\langle \mathbb{I}_d | \quad (\text{A4})$$

Consequently, for the two-qubit scenario, we have:

$$\int_{U \in SU(4)} dU \hat{U} = \frac{1}{4} |\mathbb{I}_4\rangle\rangle \langle\langle \mathbb{I}_4 | = \tilde{D}_0^{(2)} = \tilde{D}_0^{(1)} \otimes \tilde{D}_0^{(1)} \quad (\text{A5})$$

Utilizing the property of the depolarizing channel that $\tilde{D}_P^{(N)} \circ \tilde{D}_{P'}^{(N)} = \tilde{D}_{P'}^{(N)} \circ \tilde{D}_P^{(N)} = \tilde{D}_{PP'}^{(N)}$, we derive:

$$[\tilde{D}_0^{(1)} \otimes \tilde{D}_0^{(1)}, \hat{\mathbb{I}}_2 \otimes \tilde{D}_P^{(1)}] = 0 \quad \forall P \in [0, 1] \quad (\text{A6})$$

$$\Leftrightarrow \int_{U \in SU(4)} dU [\hat{U}, \hat{\mathbb{I}} \otimes \tilde{D}_P^{(1)}] = 0 \quad \forall P \in [0, 1] \quad (\text{A7})$$

This completes the proof.

Appendix B: Examples of calculating cost matrix and allocation matrix

For the swapping gates, we introduce two single-qubit depolarizing channels after each swapping gate. As is customary, we aim to position depolarizing channels at the end of the gate sequence. Although swapping gates do not commute with single-qubit depolarizing channels, a swapping gate after a single-qubit depolarizing channel moves the noise to another qubit, which allows us to directly position the depolarizing channels at the end of the circuit. Note that one may reduce the number of applied swapping gates, if one does not swap the qubits back to their original place. However, in our analysis, we adopt the approach that one immediately swaps the qubits back to their original position after the implementation of the two-qubit gate as shown in Fig. 5. This will keep the qubit allocation unchanged and let the additional swap gates form a closed swapping path.

For a multi-QPU DQC device, we incorporate a non-local telegate employing the EJPP protocol. In that case, we need to transfer the effects of noises from auxiliary qubits to the working qubits. To this end, we introduce single-qubit depolarizing channels on both sides of the working qubits, characterized by an preserving factor of $(P_a P_{a'})^{\frac{1}{3}}$, where P_a and $P_{a'}$ represent the preserving factors of the auxiliary qubits a and a' , respectively. The proof of this noise shifting phenomenon is provided in Appendix C.

For devices comprising M auxiliary qubits and N working qubits, the cost matrix $C(q, q')$ for a gate can be determined through the following steps:

1. Identify the swapping path as per the device compiler.

2. For the swapping path that involves the EJPP protocol, eliminate the depolarizing channel on the auxiliary qubits and introduce depolarizing channels with an error parameter $(P_a P_{a'})^{\frac{1}{3}}$ on both sides of the working qubit, where P_a and $P_{a'}$ represent the error parameters of the auxiliary qubits.
3. Put all the depolarizing channels at the end of the swapping path.
4. The resulting cost matrix is an $N + M$ by $N + M$ matrix, where the component $C_{n,m}(q, q')$ denotes the number of the depolarizing channel with an error perimeter P_m acting on the qubit n , Fractions are permissible in the case of non-local gates.

To illustrate, we provide two examples of computing the cost matrix for a given swapping path. Figure 15 outlines the process for calculating the cost matrix for a local gate, with the corresponding cost matrix described by Eq. (B1) and Fig. 16 outlines the process for calculating the cost matrix for a non-local gate, with the corresponding cost matrix described by Eq. (B1). Note that, it is obvious that, the cost matrix is zero when $q = q'$.

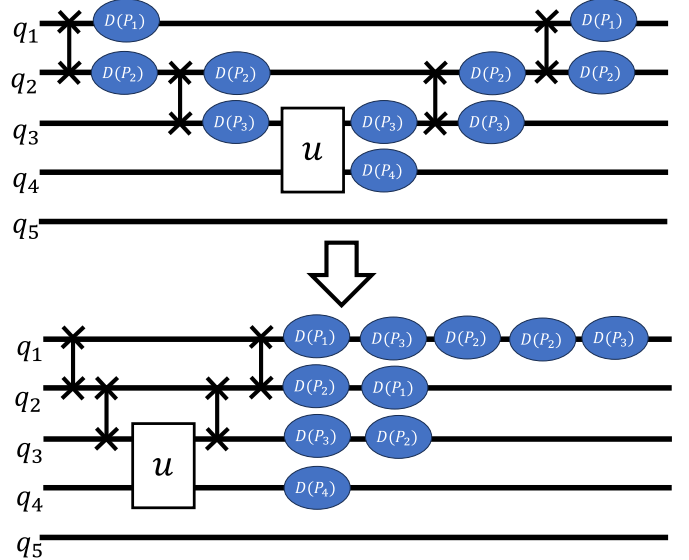


FIG. 15. Figure in the upper panel illustrates a swapping path from qubit 1 to qubit 4, as provided by the compiler, and figure in the lower panel depicts the consolidation of all depolarizing channels at the end of the swapping path. By counting the depolarizing channels on each qubit labeled with different error parameters, we determine the cost matrix $C(1, 4)$, as described by Eq. (B1).

$$C(1, 4) = \begin{bmatrix} 1 & 2 & 2 & 0 & 0 \\ 1 & 1 & 0 & 0 & 0 \\ 0 & 1 & 1 & 0 & 0 \\ 0 & 0 & 0 & 1 & 0 \\ 0 & 0 & 0 & 0 & 0 \end{bmatrix} \quad (\text{B1})$$

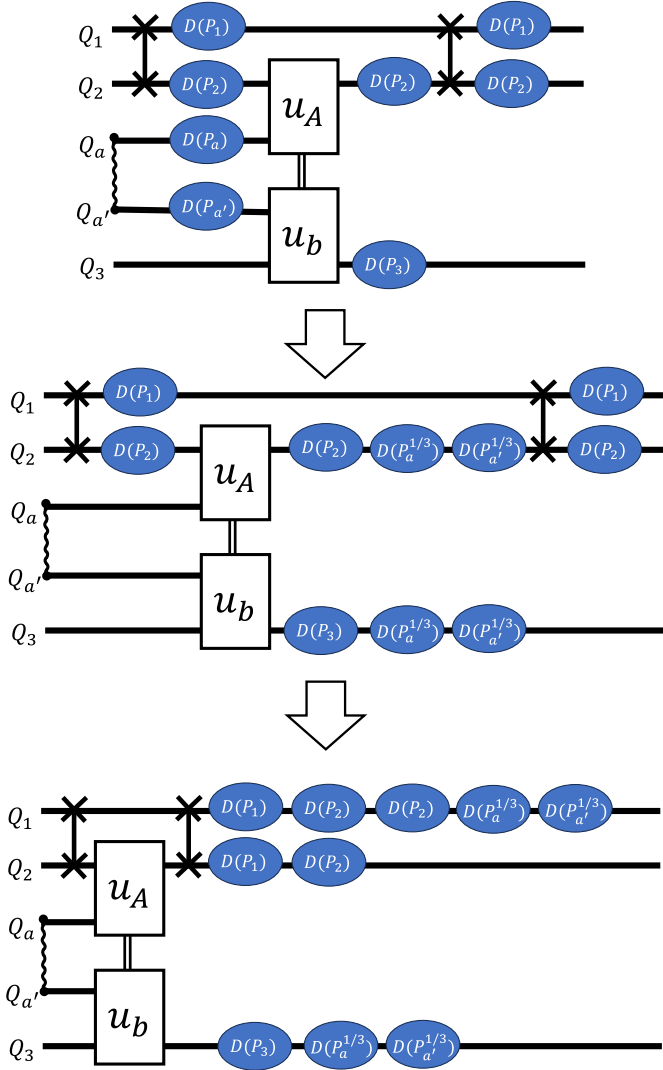


FIG. 16. The figure in the top panel illustrates a swapping path from qubit 1 to qubit 3 involving EJPP protocol, the figure in the middle panel demonstrates the error shifting process from auxiliary qubits to working qubits, and the figure in the bottom panel depicts the consolidation of all depolarizing channels at the end of the swapping path. Through this process, we derive the cost matrix $C(1,3)$, as described by Eq. (B2)

$$C(1,3) = \begin{bmatrix} \frac{1}{3} & \frac{1}{3} & 1 & 2 & 0 \\ 0 & 0 & 1 & 1 & 0 \\ \frac{1}{3} & \frac{1}{3} & 0 & 0 & 1 \end{bmatrix} \quad (\text{B2})$$

We define the allocation matrix A as the average of the cost matrix of all possible gates:

$$A \equiv \frac{1}{2(N-1)} \sum_{q,q' \in Q_w} C(q,q') \quad (\text{B3})$$

The connectivity of the devices and the allocation algorithm of the compiler are encapsulated within the allocation matrix $A_{q,q'}$.

Appendix C: Error shifting in the EJPP protocol

When considering the depolarizing channel acting on the auxiliary qubits, one can first shift it to the beginning of the circuit, resulting in the entangled state:

$$\rho_{\Phi^+}(F_e) = F_e |\Phi^+\rangle\langle\Phi^+| + \frac{1-F_e}{4} \mathbb{I}_4 \quad (\text{C1})$$

where the $F_e = P_a P_{a'}$. Consequently, the channel of the EJPP protocol circuit can be treated as a convex combination with a perfect part ($|\Phi^+\rangle\langle\Phi^+|$) and a completely mixed part ($\frac{1}{4}\mathbb{I}_4$). The perfect part yields the desired CONT gate, while the channel of the completely mixed part is given by:

$$\widetilde{CX} = (\frac{1}{2}\hat{\sigma}_0 + \frac{1}{2}\hat{\sigma}_3) \otimes (\frac{1}{2}\hat{\sigma}_0 + \frac{1}{2}\hat{\sigma}_1) \quad (\text{C2})$$

Where $\{\sigma_i\}_i$ is the set of the Pauli operators. With the consideration of the KAK decomposition, if one commutes the channel of the completely mixed part with the local unitary gates, the $\hat{\sigma}_0$ remains unchanged, but the $\hat{\sigma}_n$ ($n = 1$ or 3) changes direction, becoming a linear combination of the Pauli operator, *i.e.*, $u\sigma_i u^\dagger = \vec{n} \cdot \vec{\sigma}$. Consequently, after averaging the possible unitaries, we obtain:

$$\begin{aligned} \tilde{\sigma}_{avg} &= \int_U du \hat{u} \circ \hat{\sigma}_i \circ \hat{u}^\dagger = \int_{|\vec{n}|=1} d\vec{n} \vec{n} \cdot \vec{\sigma} \otimes \vec{n} \cdot \vec{\sigma}^* \\ &= \frac{1}{3} \sum_{i=1}^3 \hat{\sigma}_i \end{aligned} \quad (\text{C3})$$

$$\begin{aligned} \widetilde{CX}_{avg} &= \iint_{U_a, U_b} du_a du_b (\hat{u}_a \otimes \hat{u}_b) \circ \widetilde{CX} \circ (\hat{u}_a^\dagger \otimes \hat{u}_b^\dagger) \\ &= (\frac{1}{3}\hat{\sigma}_0 + \frac{2}{3}(\frac{\sum_{i=0}^3 \hat{\sigma}_i}{4}))^{\otimes 2} \\ &= (\frac{1}{3}\hat{\sigma}_0 + \frac{2}{3}\tilde{D}(0))^{\otimes 2} \end{aligned} \quad (\text{C4})$$

Here we used a relation that $\tilde{D}_P^{(1)} = P\hat{\sigma}_0 + \frac{(1-P)}{4} \sum_{i=0}^3 \hat{\sigma}_i$. Therefore, the total error channels should be equal to:

$$\tilde{\Lambda}(F) = F\hat{\sigma}_0^{\otimes 2} + (1-F)(\frac{1}{3}\hat{\sigma}_0 + \frac{2}{3}\tilde{D}(0))^{\otimes 2} \quad (\text{C5})$$

Then by imposing the condition of making the error separable, one gets the separable noise channel:

$$\begin{aligned} \tilde{\Lambda}(F) &\approx ((\sqrt{F} + \frac{1-\sqrt{F}}{3})\hat{\sigma}_0 + \frac{2(1-\sqrt{F})}{3}\tilde{D}(0))^{\otimes 2} \\ &= \tilde{D}(\frac{1+2\sqrt{F}}{3})^{\otimes 2} \end{aligned} \quad (\text{C6})$$

By definition $F = P_1 P_2 = (1-\epsilon_1)(1-\epsilon_2)$. Since we are dealing with nearly perfect cases ($\epsilon_{1,2} \ll 1\%$), we can simplify this to:

$$\sqrt{F} = \sqrt{(1-\epsilon_1)(1-\epsilon_2)} \approx (1 - \frac{\epsilon_1}{2})(1 - \frac{\epsilon_2}{2}) \quad (\text{C7})$$

$$\begin{aligned}\frac{1+2\sqrt{F}}{3} &\approx 1 - \frac{\epsilon_1}{3} - \frac{\epsilon_2}{3} \approx (1-\epsilon_1)^{\frac{1}{3}}(1-\epsilon_2)^{\frac{1}{3}} \\ &= P_1^{\frac{1}{3}} P_2^{\frac{1}{3}}\end{aligned}\quad (\text{C8})$$

Here we calculate the error for a single EJPP protocol circuit, and for a SU(4) gate, three EJPP protocol circuits are required. However, in our earlier discussion, we included one depolarizing channel after each two-qubit gate. Moreover, in our implementation of the local SU(4) gate, we still need to decompose it with three CNOT gates. Therefore, we have already taken into account the effect of the three EJPP protocol circuits.

Furthermore, to account for the imperfections in the pre-shared entanglement pairs, one can set the input entangled state as given in Eq. (C1) with a parameter F . Similarly, this error can be transferred to the working qubit by introducing depolarizing channels with an error parameter $F^{\frac{1}{3}}$, on each side. Regarding the allocation matrix, an additional column is required to represent the error cost caused by the non-perfect entanglement pairs.

Appendix D: Approximation of average gate fidelity

According to Eq. (39), for a small error $\epsilon_{q'}$, the effective preserving factor is approximately given by

$$\bar{P}_q = \prod_{q' \in \mathbb{Q}} (1 - \epsilon_{q'})^{A_{q,q'}} \approx 1 - \sum_{q' \in \mathbb{Q}} A_{q,q'} \epsilon_{q'}. \quad (\text{D1})$$

The average error rate ϵ is determined as

$$\langle \epsilon \rangle = \frac{1}{N} \sum_{q \in \mathbb{Q}_w} (1 - \bar{P}_q) = \frac{1}{N} \sum_{q, q' \in \mathbb{Q}_w, \mathbb{Q}} A_{q,q'} \epsilon_{q'}. \quad (\text{D2})$$

The average gate fidelity is then

$$\bar{F} \approx \prod_{q \in \mathbb{Q}_w} \left(1 - \frac{N}{2} \langle \epsilon \rangle \right) \approx \exp\left(-\frac{N^2}{2} \langle \epsilon \rangle\right). \quad (\text{D3})$$

This leads to

$$\bar{F} = \exp\left(-\frac{N}{2} \sum_{q, q' \in \mathbb{Q}_w, \mathbb{Q}} A_{q,q'} \epsilon_{q'}\right). \quad (\text{D4})$$

By further assuming that the error rate for each qubit is the same value ϵ , we get a simple formula with a characteristic value $\mathcal{A}_{\mathbb{Q}} \equiv \sum_{q, q' \in \mathbb{Q}_w, \mathbb{Q}} A_{q,q'}$ for a given QPU. In the end, the average gate fidelity is approximately given by

$$\bar{F}_{\mathbb{Q}}(\epsilon) \approx \exp\left(-\frac{N \mathcal{A}_{\mathbb{Q}}}{2} \epsilon\right). \quad (\text{D5})$$

Appendix E: Extension of fidelity estimation theory for imperfect entanglement

To incorporate the entanglement noises, one extend the construction of cost matrices by introducing single-qubit depolarizing channel D_{P_E} after the entangled state on $\{m_a, m_b\}$, as shown in Fig. 18 (a). The effective preserving factor on m_a and m_b is then p_{EP_a} and p_{EP_b} , respectively. Employing the same method derived in Appendix B, the depolarizing channel D_{P_E} is then shifted to the end of particular outputs in Fig. 18 (b). The cost matrix of the example is then extended by adding an additional column associated with the depolarizing channels originate from the entanglement pairs, which is given by

$$C(q_1, q_3) = \begin{bmatrix} 1 & 2 & 0 & 0 & \frac{1}{3} & \frac{1}{3} & \frac{1}{3} \\ 1 & 1 & 0 & 0 & 0 & 0 & 0 \\ 0 & 0 & 1 & 0 & \frac{1}{3} & \frac{1}{3} & \frac{1}{3} \\ 0 & 0 & 0 & 0 & 0 & 0 & 0 \end{bmatrix}. \quad (\text{E1})$$

-
- [1] M. Caleffi, M. Amoretti, D. Ferrari, D. Cuomo, J. Illiano, A. Manzalini, and A. S. Cacciapuoti. Distributed quantum computing: a survey, 2022.
 - [2] D. Barral, F. J. Cardama, G. Díaz, D. Faílde, I. F. Llovo, M. M. Juane, J. Vázquez-Pérez, J. Villasuso, C. Piñeiro, N. Costas, J. C. Pichel, T. F. Pena, and A. Gómez. Review of distributed quantum computing. from single qpu to high performance quantum computing, 2024.
 - [3] T. Peng, A. W. Harrow, M. Ozols, and X. Wu. Simulating large quantum circuits on a small quantum computer. *Phys. Rev. Lett.*, 125:150504, 2020.
 - [4] K. Mitarai and K. Fujii. Overhead for simulating a non-local channel with local channels by quasiprobability sampling. *Quantum*, 5:388, 2021.
 - [5] K. Mitarai and K. Fujii. Constructing a virtual two-qubit gate by sampling single-qubit operations. 23(2):023021.
 - [6] C. Piveteau, D. Sutter, and S. Woerner. Quasiprobability decompositions with reduced sampling overhead. 8(1).
 - [7] C. Piveteau and D. Sutter. Circuit knitting with classical communication. *IEEE Transactions on Information Theory*, 70(4):2734 – 2745, 2024.
 - [8] D. Gottesman and I. L. Chuang. Demonstrating the viability of universal quantum computation using teleportation and single-qubit operations. *Nature*, 402:390–393, 1999.
 - [9] J. Eisert, K. Jacobs, P. Papadopoulos, and M. B. Plenio. Optimal local implementation of nonlocal quantum gates. *Physical Review A*, 62:052317, 2000.
 - [10] S. F. Huelga, J. A. Vaccaro, A. Chefles, and M. B. Plenio. Quantum remote control: Teleportation of unitary operations. *Physical Review A*, 63:042303, 2001.
 - [11] S. F. Huelga, M. B. Plenio, and J. A. Vaccaro. Remote control of restricted sets of operations: Teleportation of angles. *Physical Review A*, 65:042316, 2002.
 - [12] L. Jiang, J. M. Taylor, A. S. Sørensen, and M. D. Lukin. Distributed quantum computation based on small quan-

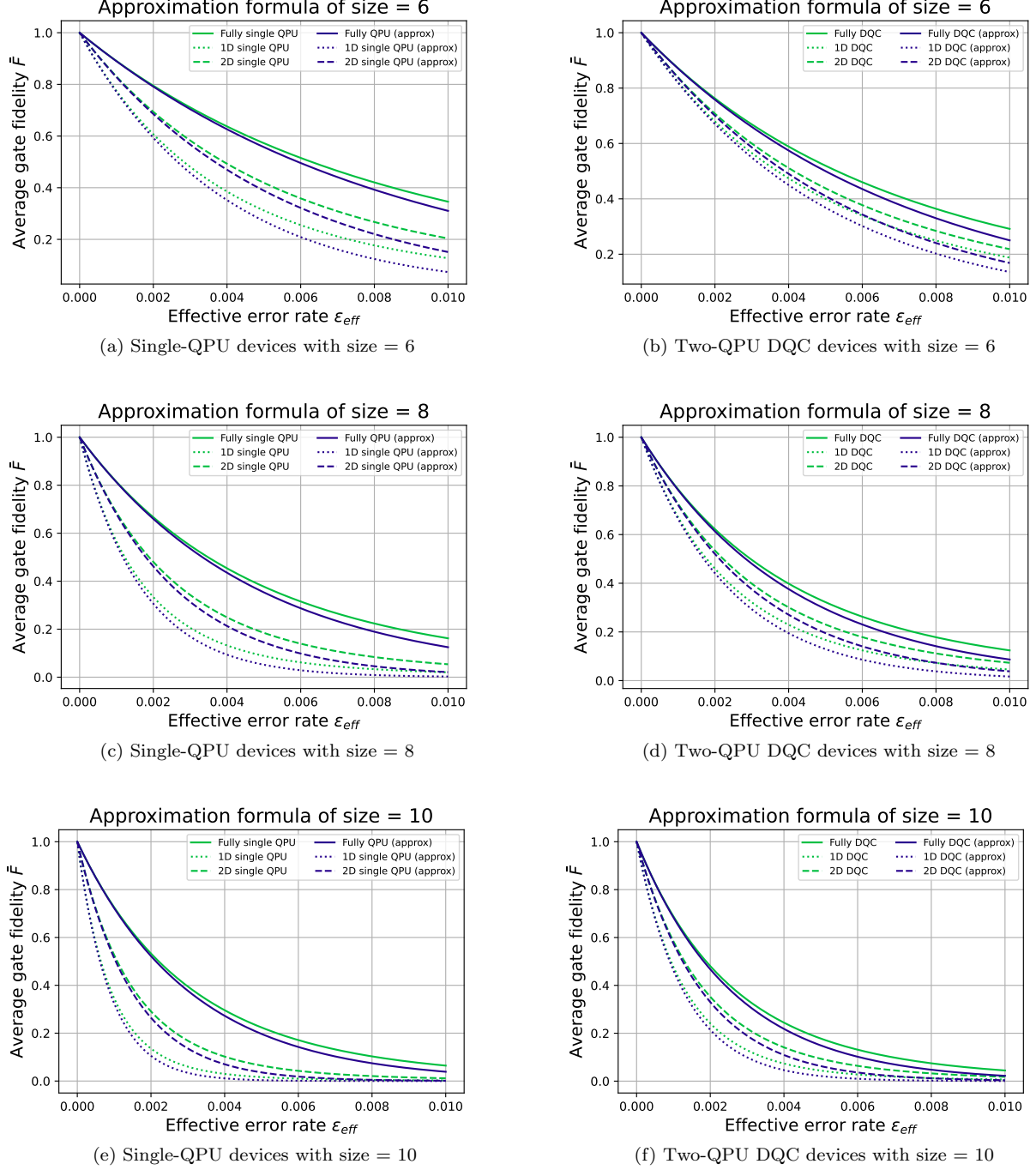


FIG. 17. The green curves stand for the original function, and the blue curves stand for the function under approximation. For size 6, although the size is not large, still we had a good match and the high-fidelity region ($\bar{F} \gtrsim 0.6$). For the larger size, the approximation gets closer to the original formula.

- tum registers. *Physical Review A*, 76:062323, 2007.
- [13] R. V. Meter, W. Munro, K. Nemoto, and K. M. Itoh. Arithmetic on a distributed-memory quantum multicomputer. *ACM Journal on Emerging Technologies in Computing Systems (JETC)*, 3(4):1–23, 2008.
- [14] R. G. Sundaram, H. Gupta, and C. R. Ramakrishnan. Efficient Distribution of Quantum Circuits. In *35th In-*

- ternational Symposium on Distributed Computing (DISC 2021)*, volume 209 of *Leibniz International Proceedings in Informatics (LIPIcs)*, pages 41:1–41:20, Dagstuhl, Germany, 2021.
- [15] J.-Y. Wu, K. Matsui, T. Forrer, A. Soeda, P. Andrés-Martínez, D. Mills, L. Henaut, and M. Murao. Entanglement-efficient bipartite-distributed quantum

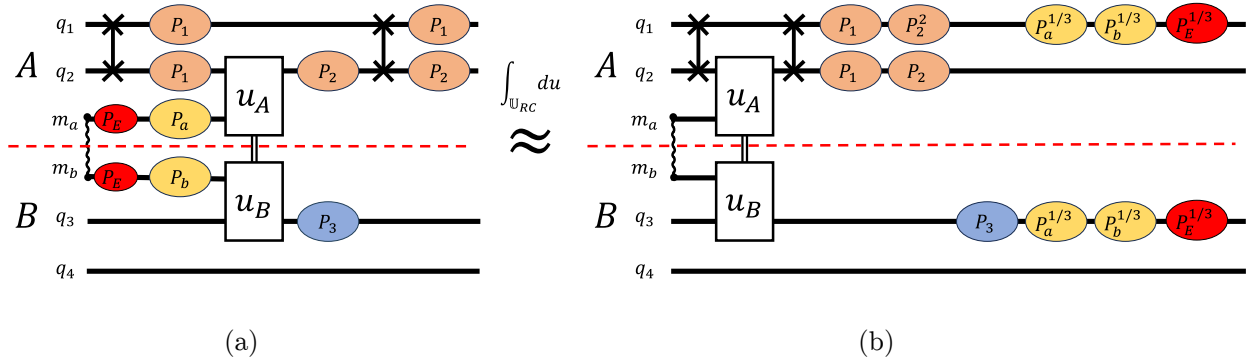


FIG. 18. Cost matrix with entanglement noise. The red circles are the depolarizing noises of the entangled pair.

- computing. *Quantum*, 7:1196, 2023.
- [16] P. Andres-Martinez, T. Forrer, D. Mills, J.-Y. Wu, L. Henaut, K. Yamamoto, M. Murao, and R. Duncan. Distributing circuits over heterogeneous, modular quantum computing network architectures. *arXiv:2305.14148*.
- [17] K. Życzkowski and H.-J. Sommers. Average fidelity between random quantum states. *Physical Review A*, 71:032313, 2005.
- [18] A. W. Cross, L. S. Bishop, S. Sheldon, P. D. Nation, and J. M. Gambetta. Validating quantum computers using randomized model circuits. *Physical Review A*, 100:032328, 2019.
- [19] F. Arute, K. Arya, R. Babbush, D. Bacon, J. C. Bardin, R. Barends, R. Biswas, S. Boixo, F. G. S. L. Brandao, D. A. Buell, B. Burkett, Y. Chen, Z. Chen, B. Chiaro, R. Collins, W. Courtney, A. Dunsworth, E. Farhi, B. Foxen, A. Fowler, C. Gidney, M. Giustina, R. Graff, K. Guerin, S. Habegger, M. P. Harrigan, M. J. Hartmann, A. Ho, M. Hoffmann, T. Huang, T. S. Humble, S. V. Isakov, E. Jeffrey, Z. Jiang, D. Kafri, K. Kechedzhi, J. Kelly, P. V. Klimov, S. Knysh, A. Korotkov, F. Kostrița, D. Landhuis, M. Lindmark, E. Lucero, D. Lyakh, S. Mandrà, J. R. McClean, M. McEwen, A. Megrant, X. Mi, K. Michielsen, M. Mohseni, J. Mutus, O. Naaman, M. Neeley, C. Neill, M. Y. Niu, E. Ostby, A. Petukhov, J. C. Platt, C. Quintana, E. G. Rieffel, P. Roushan, N. C. Rubin, D. Sank, K. J. Satzinger, V. Smelyanskiy, K. J. Sung, M. D. Trevithick, A. Vainsencher, B. Villalonga, T. White, Z. J. Yao, P. Yeh, A. Zalcman, H. Neven, and J. M. Martinis. Quantum supremacy using a programmable superconducting processor. *Nature*, 574(7779):505–510, 2019.
- [20] S. Aaronson and L. Chen. Complexity-theoretic foundations of quantum supremacy experiments. In *Proceedings of the 32nd Computational Complexity Conference, CCC '17*, Dagstuhl, DEU, 2017. Schloss Dagstuhl–Leibniz-Zentrum fuer Informatik.
- [21] M. A. Nielsen. A simple formula for the average gate fidelity of a quantum dynamical operation. 303(4):249–252.
- [22] C. H. Bennett, G. Brassard, C. Crépeau, R. Jozsa, A. Peres, and W. K. Wootters. Teleporting an unknown quantum state via dual classical and einstein-podolsky-rosen channels. *Physical Review Letters*, 70:1895–1899, 1993.
- [23] A. A. Mele. Introduction to Haar Measure Tools in Quantum Information: A Beginner’s Tutorial.
- [24] G. M. D’Ariano, G. Chiribella, and P. Perinotti. *Quantum Theory from First Principles: An Informational Approach*. Cambridge University Press, 2017.
- [25] Y. Mao, Y. Liu, and Y. Yang. Qubit allocation for distributed quantum computing. In *IEEE INFOCOM 2023 - IEEE Conference on Computer Communications*. IEEE.
- [26] R. Kukulski, I. Nechita, u. Pawela, Z. Puchała, and K. Życzkowski. Generating random quantum channels. 62(6):062201.